International Journal of Nanomedicine

Dovepress
open access to scientific and medical research

Open Access Full Text Article

ORIGINAL RESEARCH

A New Nanoplatform Under NIR Released ROS Enhanced Photodynamic Therapy and Low Temperature Photothermal Therapy for Antibacterial and Wound Repair

Licai Miao[1,*], Zihao Xu[1,*], Junhao Sui[1,*], Xiangyu Meng[1,*], Shicheng Huo[2], Shu Liu[1], Mengchen Chen[1], Zhong Zheng[1], Xiaobin Cai[3], Hao Zhang[1]

[1]Department of Orthopedics, Changhai Hospital Affiliated to the Navy Military Medical University, Shanghai, 200433, People's Republic of China; [2]Department of Orthopedic Surgery, Spine Center, Changzheng Hospital, Navy Medical University, Shanghai, 200003, People's Republic of China; [3]Department of Orthopedics Shanghai Tenth People's Hospital Tongji University School of Medicine, Shanghai, 200072, People's Republic of China

*These authors contributed equally to this work

Correspondence: Xiaobin Cai, Department of Orthopedics Shanghai Tenth People's Hospital Tongji University School of Medicine, Shanghai, 200072, People's Republic of China, Tel +8613122575295, Email caixbjn@163.com; Hao Zhang Department of Orthopedics, Changhai Hospital Affiliated to the Navy Military Medical University, Tel +8613917856377, Email zhanghsmmu@126.com

Purpose: Skin injury, often caused by physical or medical mishaps, presents a significant challenge as wound healing is critical to restore skin integrity and tissue function. However, external factors such as infection and inflammation can hinder wound healing, highlighting the importance of developing biomaterials with antibiotic and wound healing properties to treat infections and inflammation. In this study, a novel photothermal nanomaterial (MMPI) was synthesized for infected wound healing by loading indocyanine green (ICG) on magnesium-incorporated mesoporous bioactive glass (Mg-MBG) and coating its surface with polydopamine (PDA).

Results: In this study, Mg-MBG and MMPI was synthesized via the sol-gel method and characterized it using various techniques such as scanning electron microscopy (SEM), the energy dispersive X-ray spectrometry (EDS) system and X-ray diffraction (XRD). The cytocompatibility of MMPI was evaluated by confocal laser scanning microscopy (CLSM), CCK8 assay, live/dead staining and F-actin staining of the cytoskeleton. The antibacterial efficiency was assessed using bacterial dead-acting staining, spread plate method (SPM) and TEM. The impact of MMPI on macrophage polarization was initially evaluated through flow cytometry, qPCR and ELISA. Additionally, an in vivo experiment was performed on a mouse model with skin excision infected. Histological analysis and RNA-seq analysis were utilized to analyze the in vivo wound healing and immunomodulation effect.

Conclusion: Collectively, the new photothermal and photodynamic nanomaterial (MMPI) can achieve low-temperature antibacterial activity while accelerating wound healing, holds broad application prospects.

Keywords: infection-related wounds, magnesium-doped bioactive glass, photothermal therapy, photodynamic therapy, immunomodulation

Introduction

The skin is the largest organ of the human body and serves as the first line of defense against pathogen invasion.[1] However, physical, chemical, or mechanical factors often cause skin damage, resulting in wounds that affect the integrity and function of the skin and tissues. The healing of skin wounds is a complex process, including hemostasis, inflammation, proliferation, and remodeling, involving the coordinated action of various cells, tissues, and biological factors.[2] Most skin wounds heal within one to two weeks, but infected skin wounds can lead to serious complications, such as severe pain, amputation, or even death.[3] Therefore, bacterial infection is one of the greatest obstacles to wound healing. To treat infected wounds, a variety of methods have been developed. Traditional therapies primarily involve the use of medications (such as implant

Received: 30 May 2024
Accepted: 17 July 2024
Published: 24 July 2024

extracts, antibiotics, etc). Unfortunately, these methods have certain limitations to varying degrees.[4] For example, steroid medications used during the anti-inflammatory process not only suppress the immune system but also inhibit collagen synthesis and fibroblast proliferation. Excessive reliance on antibiotics not only causes severe hepatorenal toxicity but also leads to the emergence of antibiotic-resistant bacteria, resulting in chronic wounds that are difficult to heal, and can even be life-threatening.[5] Therefore, there is an urgent need to develop new therapies to treat infected wounds.

Photothermal therapy (PTT) is a non-invasive, safe, controllable, and broadly promising technology.[6] It utilizes photothermal agents (PTAs) to convert light energy into heat energy, generating localized high temperatures that disrupt the complete structure of bacteria, thus eliminating them and promoting wound healing.[7,8] At present, there are many kinds of photothermal materials with excellent antibacterial properties, such as noble metal nanoparticles, metal compound nanomaterials and organic nanomaterials.[9–12] However, in the typical thermal treatment process of PTT, high doses of PTAs inevitably damage the surrounding healthy tissues, thereby affecting wound healing.[13] Fortunately, mild PTT (at temperatures around 45°C) does not damage the wound tissue, and can also improve local blood circulation, promote fibroblast proliferation and collagen synthesis, enhance tissue repair and regeneration capabilities, thereby accelerating wound healing.[14,15] In this regard, development of a biomaterial that has a mild PTT effect is likely to substantially promote the healing of wounds that are associated with infection.[16] Polydopamine (PDA) is an organic polymer material with photothermal effects, generating heat by absorbing near-infrared light.[17] PDA is fully biodegradable in the body, possessing high biocompatibility and photothermal conversion efficiency.[18] PDA can also be mixed with other materials, offering enhanced stability, antibacterial properties, and promoting tissue repair.[19] More importantly, PDA exhibits a mild photothermal effect.[20] Indocyanine green (ICG) is an important near-infrared (NIR) photosensitive molecule, used in PTT/PDT therapy and imaging.[21] It generates reactive oxygen species (ROS), capable of killing pathogenic bacteria under near-infrared irradiation.[22] Composite nanomaterials based on ICG have been designed and widely applied, especially in the fields of oncology and antimicrobial therapy.[23]

Mesoporous bioactive glass (MBG) is a third-generation biomaterial, with research in tissue repair burgeoning in recent years.[24] This series of materials promotes tissue repair by altering the microenvironment of the extracellular matrix through the production of dissolution and degradation products.[25] Mesoporous bioactive glass containing Mg^{2+} (Mg-MBG) is a new type of therapeutic nanosphere with good biocompatibility. On one hand, its mesoporous structure can encapsulate drugs or other molecules; on the other hand, due to its solubility and stability, it can serve as an excellent carrier for antimicrobial substances.[26] As previously mentioned, wound infections prompt macrophages to polarize towards M1, producing a plethora of inflammatory factors, severely inhibiting tissue repair.[27] Fortunately, Mg^{2+} can promote macrophages to polarize towards M2, mitigating the inflammatory response, participating in various wound healing processes, thus accelerating wound healing and promoting tissue repair.[28,29]

Consequently, a novel nanoplatform (MMPI) was fabricated in the present study for combined photothermal and photodynamic therapy, encapsulating PDA onto Mg-MBG and loading ICG via π-π stacking. Under NIR irradiation, MMPI generates a temperature of approximately 45 °C in wound tissues, avoiding damage to healthy tissues from high temperatures and stimulating vascular and fibroblast proliferation to promote wound healing. Furthermore, this temperature increases the permeability of bacterial cell membranes, making them more sensitive and vulnerable. Simultaneously, the heat generated by MMPI facilitates the release of ICG and the production of ROS, destroying bacterial cell membranes that are already sensitive to photothermal effects, thereby killing the bacteria. Concurrently, the release of Mg^{2+} promotes the polarization of macrophages towards M2, mitigating the inflammatory response and participating in the wound repair process, accelerating wound healing. In summary, MMPI enhances PDT by promoting the release of ROS from ICG, achieving the ability to kill bacteria under mild PTT conditions, and accelerates wound healing through the release of Mg^{2+}. The preparation process and action mechanism of MMPI are illustrated in the Scheme 1.

Materials and Methods

Materials

Chemicals including dopamine hydrochloride, tris(hydroxymethyl) aminomethane (Tris, 99.9%), and 1,3,5-trimethylbenzene (TMB, 97%) were procured from Aladdin Industrial Co. Additionally, Indocyanine green (ICG, 98%) was obtained from All J&K Scientific Co., and fetal bovine serum (FBS, Sigma-Aldrich) was acquired from Sigma-Aldrich.

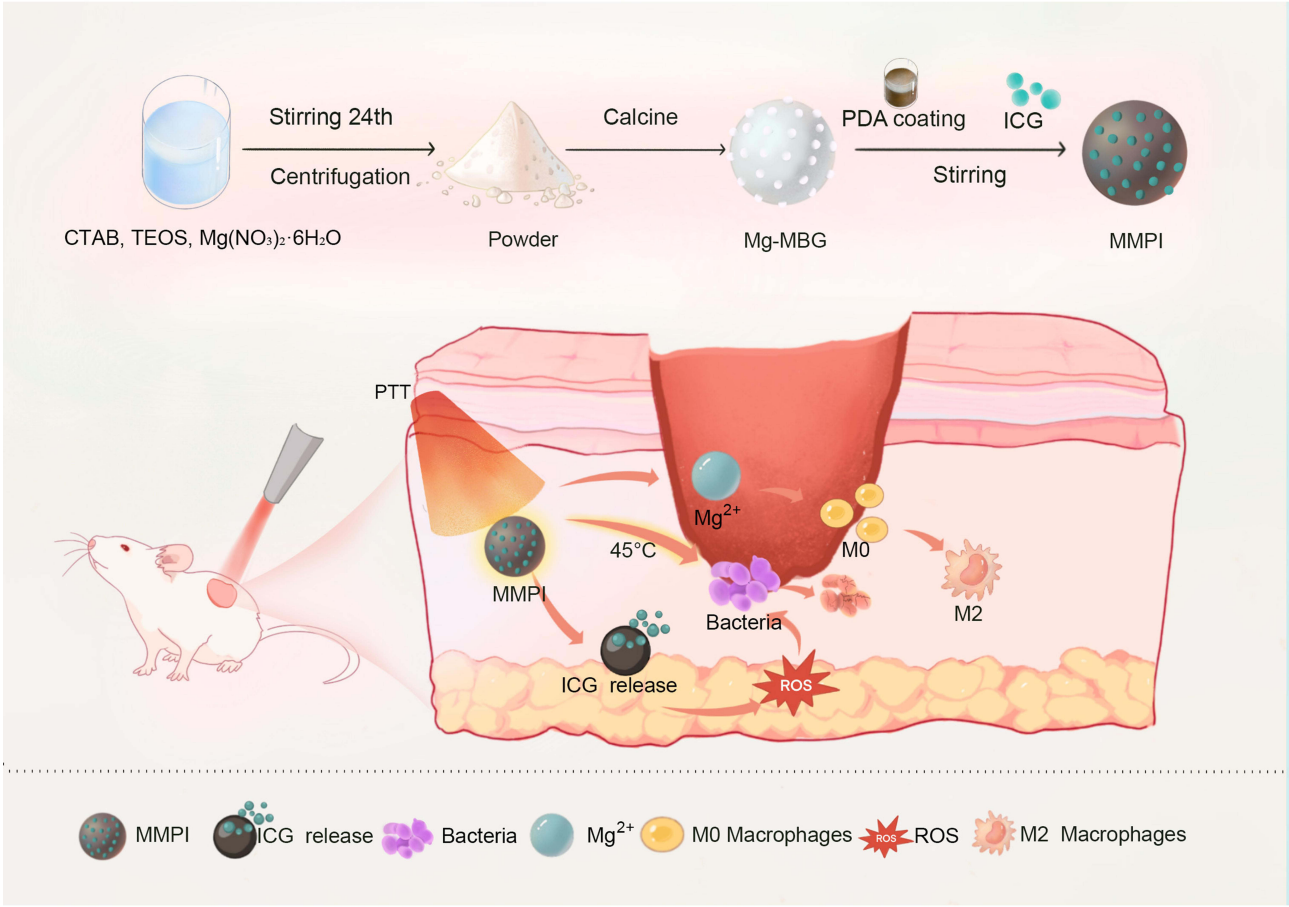

Scheme 1 The synthesis process of MMPI and the mechanism for antibacterial and immunomodulation.

Synthesis of MMPI Nanoparticles

The Mg-MBG was synthesized via the sol-gel method with a Mg content of 5%.[30] Subsequently, ICG was combined with a DA solution (1 mg/mL, pH = 8.5), followed by the addition of the Mg-MBG sample and overnight stirring to achieve PDA coating and facilitate complete ICG loading into the Mg-MBG through π-π stacking interactions. The resulting composite, termed as the Mg-MBG/ICG/PDA composite (MMPI), was separated by centrifugation.

Characterization

Scanning electron microscopy (SEM, S4800, Hitachi) and Transmission Electron Microscopy (TEM, JEM2100, Hitachi) were utilized for the observation of nanoparticle morphology and size. The energy dispersive X-ray spectrometry (EDS) system and X-ray photoelectron spectroscopy (XPS, Phi V5000) were employed for the detection of element composition in Mg-MBG and MMPI. Fourier transform infrared spectrometry (FTIR, Magna-IR 750, Nicolet) and X-ray diffraction (XRD, Bruker) were utilized for the determination of chemical composition and chemical state of the samples.

Photothermal Effects of Various Samples

PBS, Mg-MBG, and MMPI samples were subjected to laser irradiation at a wavelength of 808 nm with a power density of 1.5 W/cm^2 for a duration of 10 min. The temperature changes of varying concentrations of MMPI (50, 100, 200 μg/mL) were monitored during laser irradiation at the same power density. Also, temperature changes were investigated after laser irradiation at 808 nm at 0.5, 1.0, and 2.0 W/cm2 power densities. Temperature readings were taken every 30s, and a heat map was generated every 60s. The NIR laser was activated for 10 minutes, then deactivated until the material

reached room temperature before being reactivated to assess thermal stability. This process was repeated for a total of five cycles.

Then the photothermal conversion coefficient of the MMPI was calculated. The heating-cooling curve of MMPI (200 μg / mL) was obtained at 1.5 W cm^{-2}. The photothermal conversion efficiency (η) was calculated via the following formula:

$$\eta = \frac{hS(T_{max} - T_{surr} - Q_0)}{I\left(1 - 10^{-A_{808}}\right)} \tag{1}$$

$$\tau_s = \frac{m_d\ C_d}{hS} \tag{2}$$

$$Q_0 = hS\left(T_{max,\ water} - T_{surr}\right) \tag{3}$$

The value of τ_S(173.04554) can be calculated from the linear regression curve of the cooling curve, and it is the characteristic thermal time constant. m_d and C_d represent the mass (above 1g) and heat capacity (4.2 J g^{-1} K^{-1}) of the solution, respectively. Therefore, the value of hS can be obtained. Then, Q_0 is calculated by equation (3), which represents the background energy input in the absence of MMPI. Among them, $T_{max,water}$ and T_{surr} represent the maximum steady-state temperature of water (30.3°C) and normal temperature (25.1°C), respectively. Therefore, after calculating these values for hS and Q_0, the photothermal conversion efficiency (η=26.0%) can be calculated based on formula (1). T_{max} represents the stable maximum temperature of the MMPI solution (51.3°C), and *I* and A808 represent the laser power (2.0W) and the absorbance of the MMPI at 808 nm (1.7), respectively.

ROS generation was characterized with DPBF (1,3-Diphenylisobenzofuran). And the MMPI which mixed into a solution of DPBF was irradiated with an 808 nm laser (1.5 W/cm2) for 0, 2, 4, 6, 8, and 10 minutes. The absorbance of DPBF at different times was detected with an ultraviolet–visible spectrophotometer. Then the prepared MMPI was incubated at room temperature (RT) and 45°C, respectively. At various time points (2, 4, 6, 12, 24, 48 and 72 h), the solution was removed for analysis and replaced with fresh PBS. The amount of ICG released was determined by fluorescence spectroscopy using a Powerwave XS spectrofluorometer.

In vitro Cytocompatibility Evaluation

Cytotoxicity

The NIH-3T3 cells were obtained from the Shanghai Institute of Cell Biology.And cells (NIH-3T3, 200 μL, 1×10^4 cells/well) were initially plated in 48-well plates and allowed to incubate for 24 h. Various samples were then introduced to the plates and co-cultured with the cells for 24 and 48 h, with pure PBS serving as the control group. Subsequently, the culture medium was aspirated, and a 200 μL mixture solution of fresh medium containing CCK-8 solution (v/v = 10:1) was added to each well. Following a 2-h incubation at 37°C, the absorbance values at 450 nm of all supernatants were measured using a spectrophotometric microplate reader (Bio-Rad 680, USA).

Cell Morphology and Cytoskeleton

The NIH-3T3 cells (1×10^4 cells/well) were co-cultured with various samples for one day, followed by fixation with paraformaldehyde. Actin staining was performed using FITC-Phalloidin (10 μL/well), while DAPI (5 μg/mL) was utilized for nuclear staining, and the specimens were observed using confocal laser scanning microscopy (CLSM).

Cell Dead and Alive Staining

Following a 1-day incubation period with various samples, NIH-3T3 cells (1×104 cells/well) were stained with 500 μL of a combination dye (Calcein AM and PI) and subsequently analyzed qualitatively using CLSM. Dead cells exhibiting compromised plasma membranes emitted red fluorescence, while viable cells displaying esterase activity emitted green fluorescence.[31,32]

In vitro Antibacterial Assays

Bacterial Strains

The MRSA and E. coli strains were inoculated into tryptic soy broth (TSB; Hope Bio) and incubated under shaking at 37°C overnight. The bacterial cultures were subsequently diluted 1:10,000 in TSB to achieve exponential growth and incubated for 4–6 h. Following this, the bacteria were exposed to various nanoparticles at a concentration of 100 μg/mL, and subsequently subjected to irradiation with or without NIR.

In vitro Antibacterial Efficiency

The in vitro antimicrobial activity of MMPI was assessed using the spread plate method (SPM). Specifically, 100 μL of the co-cultured solution was evenly spread on agar plates and incubated at 37°C for 18 h. The resulting colony forming units (CFU) on various plates were photographed and counted using Image J. Based on the CFU counts for each treatment group, the antibacterial efficiency was calculated by the following formula:

Antibacterial efficiency (%) = $(N_c–N_H) / N_c \times 100\%$.

where N_c represented colony forming units (CFUs) of PBS without NIR, N_H represented CFUs of other samples.

To further investigate the antimicrobial efficacy of MMPI, samples were treated with a combination of dyes (LIVE/DEAD BacLight Bacterial Viability Kit, Invitrogen) after 24 h of co-culture and analyzed using CLSM. Live bacteria were labeled in green, while dead bacteria were labeled in red.[33]

Tem

The alterations in the ultrastructure of the bacterial membrane were examined using TEM. The bacteria were subjected to fixation in 1mL of fixative and treated with osmium tetroxide. Subsequently, the bacteria underwent dehydration, embedding in a gradient concentration of ethanol, and sectioning with a diamond knife. The sections were mounted on reticulated copper grids, stained with lead citrate, and observed under TEM.

ROS Release

The ROS Assay Kit (DCFH-DA) was purchased from Beyotime Biotech Inc.The diluted strains of MRSA and E. coli were inoculated into separate wells of 48-well plates containing various samples, followed by exposure to NIR irradiation. The samples were subsequently stained using DCFH-DA and qualitatively analyzed using CLSM, and analyzed the statistical differences by Prism 10 and image J.

Macrophage Polarization

Cell Culture

The RAW 264.7 cell line was procured from the cell bank at the Chinese Academy of Sciences. The cells were cultured in α-MEM medium supplemented with 10% FBS and incubated at 37°C with 5% CO_2 for maintenance.

Flow Cytometry

Lipopolysaccharide (LPS) was introduced to all experimental groups with the exception of the control group treated with pure PBS. Subsequently, the cells were co-cultured with various samples for a duration of 24 h. Following centrifugation, the cells were stained with phycoerythrin (PE)-conjugated CD206 (PE; Biolegend, cat. no. 141706, clone C068C2) and allophycocyanin (APC)-conjugated CD11c (APC; Biolegend, cat. no. 117310, clone N418). The resulting cell suspensions were then subjected to analysis using flow cytometry.

qPCR and ELISA

The cells were processed and collected in accordance with the aforementioned protocol, followed by RNA extraction using TRIzol reagent and reverse transcription reactions conducted using the PrimeScript RT kit (Takara) as per the manufacturer's guidelines. The primer sequences utilized for PCR analysis can be found in Table 1. Furthermore, ELISA assays (R&D systems) were performed on cell culture supernatants to measure levels of TNF-α, IL-8, iNOS, and IL-10.

Table 1 Primers Used in This Assay

Gene and primer direction	Primer sequence (5′to 3′)
Mouse TNF-α	
Forward	CCCTCACACTCAGATCATCTTCT
Reverse	GCTACGACGTGGGCTACAG
Mouse iNOS	
Forward	GTTCTCAGCCCAACAATACAAGA
Reverse	GTGGACGGGTCGATGTCAC
Mouse IL-10	
Forward	GGCTGGACGAGAGCCGAACG
Reverse	CCCGGGGTGTAGGCACCACT
Mouse IL-8	
Forward	GCTGTTACTGCCACGGCACAGT
Reverse	CACCATCCTTTTGCCAGTTCCTCC

Antimicrobial Experiments in vivo

Mouse Skin Wound Infection Model

The animal experimental procedures were adhered to the National Institutes of Health (NIH) Guide for the Care and Use of Laboratory Animals, and approved by the Animal Ethics Committee of the Naval Military Medical University. A total of 48 male BALB/c mice, aged 6 weeks and weighing 25–30 g, were randomly allocated to six groups: PBS group (with and without NIR), Mg-MBG group (with and without NIR), and MMPI group (with and without NIR). Following intraperitoneal anesthesia with 3% pentobarbital, mice underwent shaving, disinfection, and the creation of a 1 cm diameter skin wound on their backs. A combination of bacteria and material was subsequently applied to the wound site. The NIR group received exposure to a NIR laser for 10 minutes (808 nm, 1.5 W/cm^2). Thermal imaging using an infrared camera was conducted, and daily observations were made regarding the progression of the skin wounds in the mice.

Histological Analysis

On day 10, the mice in each experimental group were euthanized, and their skin wounds and surrounding tissues were harvested and subsequently preserved in 4% formaldehyde solution. Histological examination of the specimens was conducted through hematoxylin and eosin (HE) and Masson's trichrome staining to assess pathological alterations. Immunofluorescence staining was utilized to detect macrophages in the skin tissues, which were then visualized using CLSM.[34] Green (iNOS, M1 macrophages marker): Anti-iNOS antibody [EPR16635] - Mouse IgG2b (Chimeric) (ab210823), followed by Goat Anti-Mouse IgG H&L (FITC) (ab6785) (secondary antibody). Red (CD206, M2 macrophages marker): Anti-Mannose Receptor antibody (ab64693), Goat Anti-Rabbit IgG H&L (Cy3 ®) preadsorbed (ab6939) (secondary antibody), and blue (DAPI): Mounting Medium With DAPI (ab104139). All antibodies were purchased from Abcam Plc. The wound tissues were collected to measure the levels of iNOS, IL-6, TNF-α and IL-10 according to the previous method.

RNA-Seq Analysis

Following the collection of the aforementioned tissues, total RNA extraction was carried out utilizing TRIzol reagent, followed by RNA-seq and bioinformatics analyses conducted by Suzhou PANOMIX Biomedical Tech Co Ltd. Differential expressed genes (DEGs) were then subjected to analysis for KEGG pathway and gene ontology enrichment.

Statistical Analysis

Numeric data were reported as mean ± standard deviation (SD), unless specified otherwise. A two-tailed Student's *t*-test was used to compare two groups, while multiple comparisons were conducted using one-way analysis of variance (ANOVA). Excel 2016 and GraphPad Prism 10 were used for all calculations and statistical analyses. Statistical significance was set at $P < 0.05$.

Results and Discussion

Characterization

TEM were utilized for the examination of the morphology of the synthesized Mg-MBG and MMPI materials (Figure 1A). The average particle size of Mg-MBG is approximately 100 nm, exhibiting a uniform mesoporous structure. In contrast, the average particle size of MMPI is around 120 nm, and its mesoporous structure is no longer visible after the incorporation of ICG. The outermost annular structure confirms the effective coating with PDA. TEM-EDS images demonstrate the presence of Mg, O, and Si in both Mg-MBG and MMPI. Additionally, the detection of nitrogen (N) in MMPI suggests the successful encapsulation with PDA.[35] Figure 1B displayed the FT-IR spectra of Mg-MBG and MMPI, with the bands at 798 cm^{-1} and 1089 cm^{-1} associated with Si-O-Si bending and Si-O-Si stretching, respectively. The bands of PDA nanoparticles appearing at 1509 cm^{-1} was ascribed to the N-H bending

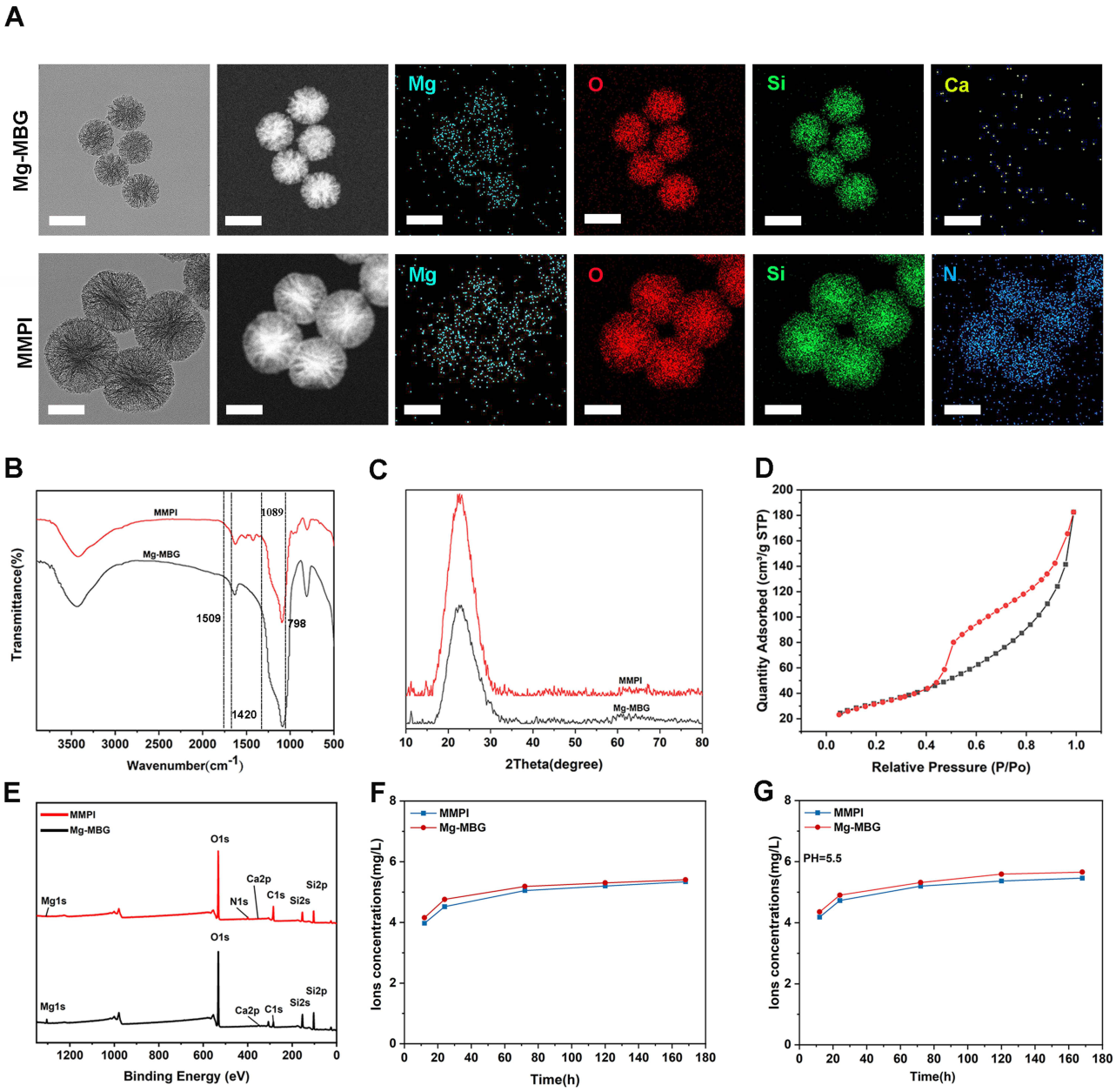

Figure 1 Characterization of the Mg-MBG and MMPI. (**A**) SEM and TEM-EDS images of Mg-MBG and MMPI. Scale bar: 100 nm. (**B**) FTIR spectra,(**C**) XRD patterns, (**D**) Pore-size distribution, (**E**) XPS spectrum, and (**F** and **G**) the concentrations of Mg^{2+} as determined by ICP-OES of Mg-MBG and MMPI.

vibrations, C=C resonance vibrations in the aromatic ring, and O-H stretching vibrations. As can be seen from MMPI, new absorption peaks appeared at 1420 cm^{-1}, assigned to characteristic peaks of ICG, indicating that the MMPI was successfully loaded with ICG.[36,37] The XRD spectrum (Figure 1C) revealed a broad halo at 2θ=20°-30°, suggesting the presence of an amorphous phase in the Mg-MBG and MMPI material. The N2 adsorption-desorption isotherms of Mg-MBG displayed type IV isotherm characteristics, suggesting a mesoporous structure of Mg-MBG (Figure 1D), with a BET surface area of 293.86 m^2/g. The component and valence states of Mg-MBG and MMPI were tested by X-ray photoelectron spectroscopy (XPS, Figure 1E). The elements including Mg, O, N, Ca, and Si were detected, which was consistent with the TEM-EDS images. The gradual increase in the release of magnesium ions from Mg-MBG and MMPI over a seven-day period, with a notable spike at 24 h, resulted in total releases of 5.4065 and 5.341 mg/L on the seventh day, respectively (Figure 1F). In order to better demonstrate the release of Mg^{2+} in composite, we simulated the wound environment and measured the release of Mg^{2+} over a seven-day period in PBS solution with PH=5.5. The results showed that the composite was also effective in releasing Mg^{2+} in the simulated wound environment (Figure 1G). These findings suggest that MBG releases bioactive ions following the dissolution of the PDA coating in PBS.

Photothermal Investigation of MMPI

In order to assess the photothermal efficacy of the samples, PBS, Mg-MBG, and MMPI samples were subjected to irradiation with an 808 nm laser (1.5 W/cm^2) for a duration of 600 s. The results depicted in Figure 2A indicate that the temperatures of PBS and Mg-MBG remained relatively stable throughout the observation period. Conversely, the MMPI sample demonstrated notable photothermal performance, as evidenced by a rapid temperature escalation from 25°C to 45°C, attributed to the unique photothermal properties of the PDA coating, resulting in the most pronounced temperature elevation observed for the MMPI sample.[38] Moreover, the maximum attainable temperature rose from 42.5 to 51.5°C with an increase in MMPI concentration from 50 to 200 μg/mL during a 600-s exposure period (Figure 2B). In parallel, MMPI sample photothermal performance was found to be power density-dependent (Figure 2C). Within 600 s of irradiation, the temperature rose from 40.4, 45.5 and 52.3 °C in response to an increase in power density from 1 to 2 W/cm^2. Additionally, the photothermal stability of MMPI was confirmed. The data presented in Figure 2D indicates that the maximum temperature of MMPI remained relatively constant following five switching cycles, demonstrating the substance's robust photothermal stability. Based on the heating-cooling curve (Figure 2E) and corresponding thermal time constant (τ_s) (Figure 2F), the photothermal conversion efficiency (η) was ascertained to be 26.0%. As shown in Figure 2G, when DPBF was incubated with MMPI, the intensity at 410 nm displayed decrease with increasing irradiation time, which confirmed that the singlet oxygen generated by the MMPI excited by the NIR laser, indicating an effective photodynamic effect. Figure 2H shows that at room temperature (RT), only a small amount of ICG was released from MMPI. Comparatively, the release of ICG was accelerated after incubation at 45 °C and about 5.8122 μg ICG were released. Due to non-covalent interaction of π-π stacking between the aromatic regions, the connection force between ICG and MPDA is easily disrupted when surrounding temperature rises.[19,39] Infrared thermal imaging revealed that MMPI in PBS quickly reached 45.1°C after 400 s of irradiation, ultimately stabilizing at 45.8°C (Figure 2I). The IR thermal image exhibits a consistent circular pattern in orange-red hue with a diameter of 1 cm in the central area, indicating uniform surface temperature in the near-infrared spectrum. This observation underscores the exceptional photothermal performance of the MMPI attributed to the presence of the PDA coating.

Cytocompatibility Assessment in vitro

The potential toxicity of nanomaterials is a significant concern within the biomedical field.[40] As such, the cytocompatibility of MMPI was systematically evaluated in the subsequent experiments. Initially, the cytotoxicity of MMPI was assessed through the measurement of cell viability and morphology. The proliferation of 3T3 cells in various samples was then analyzed at both 24 and 48 h using CCK-8. The results depicted in Figure 3A indicate that MMPI exhibits no toxicity at concentrations of 50–100 μg/mL. However, at a concentration of 200 μg/mL, a decrease in cell viability was observed, suggesting a slight adverse effect. Figure 3B illustrates the results of 3T3 dead-viable staining, confirming the findings. Furthermore, following co-culturing with 3T3 cells for 1 day and subsequent F-actin staining of the

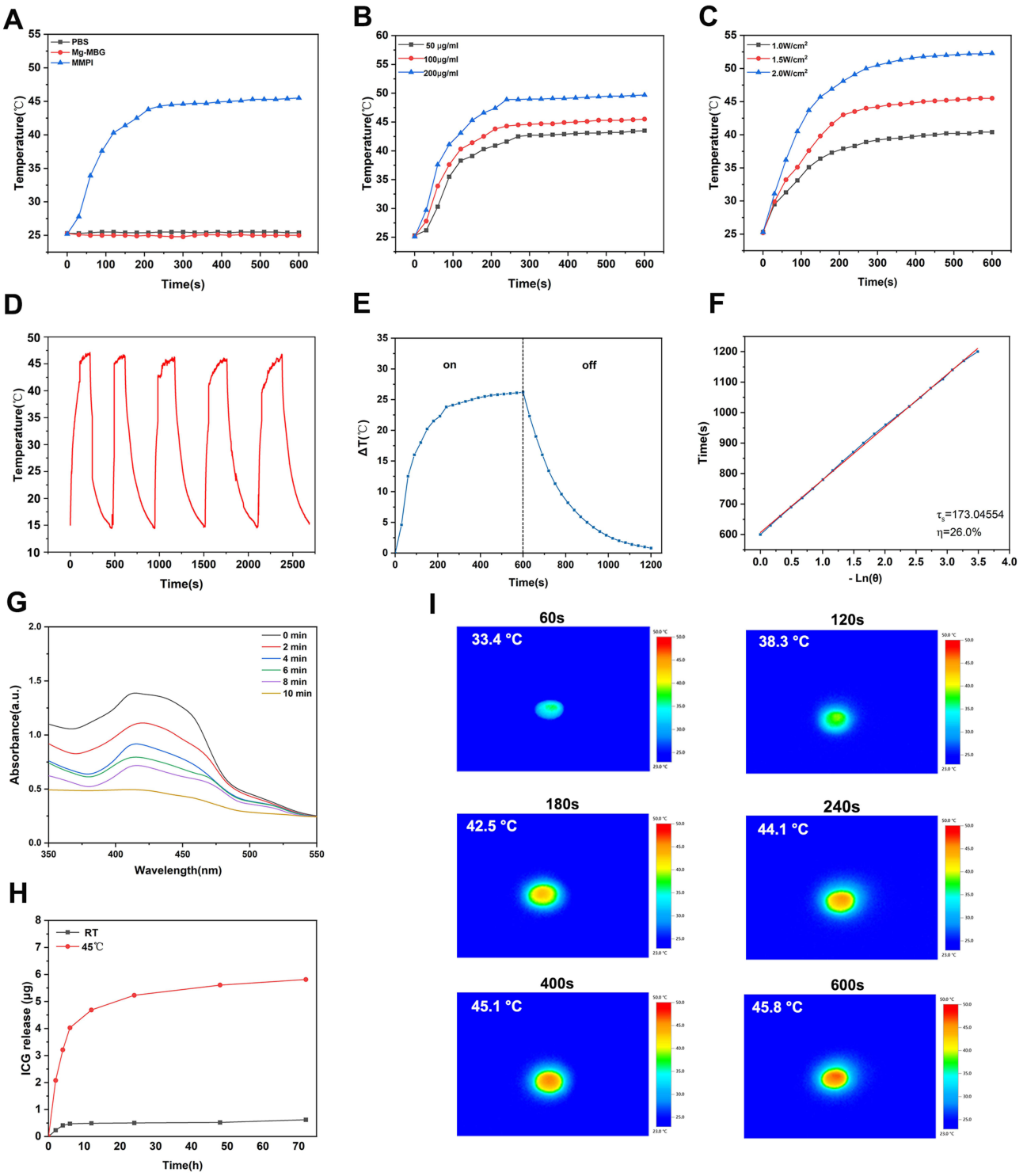

Figure 2 Photothermal performance of various nanoparticles. (**A**) Heating curves of various nanoparticles with NIR laser (1.5 W/cm^2). (**B**) Heating curves of MMPI with different concentration. (**C**) Heating curves of MMPI with different laser power densities. (**D**) Temperature changes for MMPI over five cycles of irradiation/cooling processes (100 μg/mL). (**E**) Irradiation/cooling temperature change of MMPI under laser irradiation. (**F**) Liner time data versus -Ln (θ). (**G**) Time-dependent absorbance spectra of MMPI co-incubated with DPBF after NIR irradiation. (**H**) The released ICG from MMPI at different temperatures. (**I**) Representative real-time infrared thermal images of MMPI in PBS under NIR laser irradiation (1.5 W/cm^2).

cytoskeleton, MMPI-treated cells exhibited favorable morphology and growth in comparison to control samples (Figure 3C). Ultimately, MMPI emerges as a highly biocompatible material with extensive potential for clinical utilization in wound healing owing to its exceptional biocompatibility.

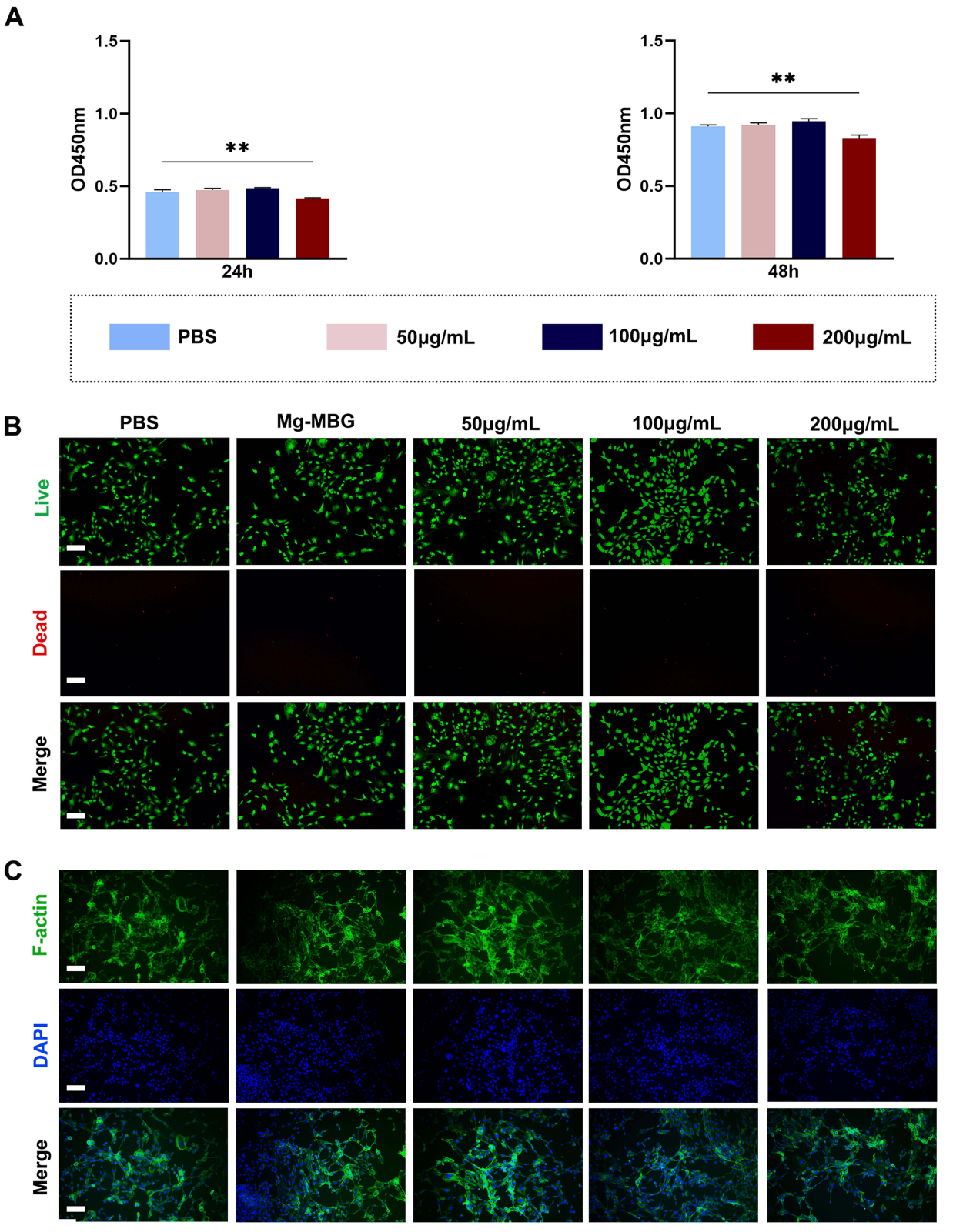

Figure 3 Cytocompatibility assessment in vitro. (**A**) Viability of NIH-3T3 treated with different dosages of MMPI for 24 h and 48 h. (**B**) Cell morphology and (**C**) The fluorescence images of living cells (green) and dead cells (red) of NIH-3T3 treated with PBS, Mg-MBG, MMPI. Scale bar: 100 μm. Data are expressed as average ± SD (n = 3). **P < 0.01.

Antibacterial Properties of MMPI in vitro

The concentration of 100 μg/mL of MMPI was selected for further studies based on its favorable photothermal properties and biocompatibility, as indicated by previous experiments. In vitro antimicrobial efficacy against MRSA and E. coli was assessed using a variety of samples. The antimicrobial activity of MMPI was confirmed through bacterial dead-acting staining, as illustrated in Figure 4A. In contrast to PBS and Mg-MBG, which exhibited no bactericidal properties when subjected to NIR laser irradiation, MMPI demonstrated notable antimicrobial effectiveness against both MRSA and E. coli. The treatment with MMPI + NIR resulted in a substantial increase in the number of deceased E. coli cells (as indicated by red fluorescence) compared to the minimal presence of live bacteria (green fluorescence). Similarly, the application of MMPI + NIR on MRSA cells led to a significant decrease in viable bacteria, underscoring the efficacy of this treatment in eradicating bacterial populations. In contrast, the results of the study indicated that MMPI exhibited significant antimicrobial efficacy against both MRSA and E. coli. The SPM and colony count outcomes results further revealed that bacterial inhibition was minimal in the absence of NIR radiation, whereas the combination of MMPI and NIR effectively deactivated both MRSA and E. coli (Figure 4B–D). Furthermore, the study examined the release of ROS by MMPI. The intensity of DCFH-DA fluorescence in the MMPI NIR+ group was higher than that in the other groups, respectively. These results were validated by fluorescence microscopy, implying that laser irradiation may augment the capacity of ICG to release ROS (Figure 4E–G). Additionally, morphological alterations in MRSA and E. coli were observed through TEM analysis. Untreated bacteria maintained their typical shape and membrane integrity, whereas bacteria treated with MMPI and NIR exhibited pronounced deformities and leakage of cytoplasm (Figure 4H).

Based on the findings presented above, the multifaceted properties of MMPI contribute to its notable antimicrobial effectiveness. Specifically, MMPI demonstrates a photothermal effect when subjected to NIR irradiation, enhancing bacterial surface permeability and sensitivity. Furthermore, localized mild hyperthermia facilitates the release of ICG, while NIR stimulation prompts the generation of ROS from the liberated ICG. Consequently, the sustained low-temperature PTT and ROS production expedite the demise of vulnerable bacteria through irreversible membrane impairment. In summary, the combined application of PDT and low-temperature PTT presents a promising approach for eradicating bacteria.

Macrophage Behavior

A well-regulated inflammatory response is crucial for facilitating tissue repair, with the immune system playing a pivotal role in this process.[41,42] Conversely, dysregulated and excessive immune responses can exacerbate tissue damage. Therefore, achieving an optimal balance in the inflammatory response is imperative for successful tissue repair.[43] Macrophages, key components of the immune system, can be polarized into M1 and M2 phenotypes in response to various stimuli. Properly polarized macrophages have the capacity to promote tissue repair effectively.

In the current investigation, the impact of MMPI on macrophage polarization was initially evaluated through flow cytometric analysis. The results depicted in Figure 5A demonstrate a decreased percentage of cells expressing CD11c in both the Mg-MBG group (16.8%) and the MMPI group (14.0%) as compared to the PBS group (2.08%) and the LPS group (32.0%). Conversely, a higher proportion of cells expressing CD206 was observed in the Mg-MBG group (9.64%) and the MMPI group (16.2%). These findings suggest a significant association between Mg-MBG and MMPI-induced macrophage polarization towards an M2 anti-inflammatory phenotype.

The inflammatory gene expression of macrophages cultured with various samples for a duration of 1 day was examined using quantitative polymerase chain reaction (qPCR) to evaluate the immunomodulatory function of MMPI (Figure 5B). In comparison to lipopolysaccharide (LPS), MMPI notably decreased the expression of M1-associated macrophage genes (TNF-α, IL-8, and iNOS), while concurrently increasing the expression of M2-associated macrophage genes (IL-10).[44,45] The aforementioned studies demonstrate that MMPI treatment led to a reduction in macrophages expressing the M1 marker CD11c and an increase in macrophages expressing the M2 marker CD206. Furthermore, the expression of inflammatory genes (eg, IL-8 and iNOS) was significantly decreased, while the anti-inflammatory gene IL-10 was upregulated following co-culture with Mg-MBG and MMPI in comparison to the PBS and LPS groups.

The phenotypic characteristics of macrophages are influenced by their inducers, properties, and surface markers. Following treatment with Mg-MBG and MMPI, macrophages exhibiting the M1 marker CD11c decreased, while those expressing the M2 marker CD206 increased. Furthermore, the expression of inflammatory genes TNF-α, IL-8, and iNOS was

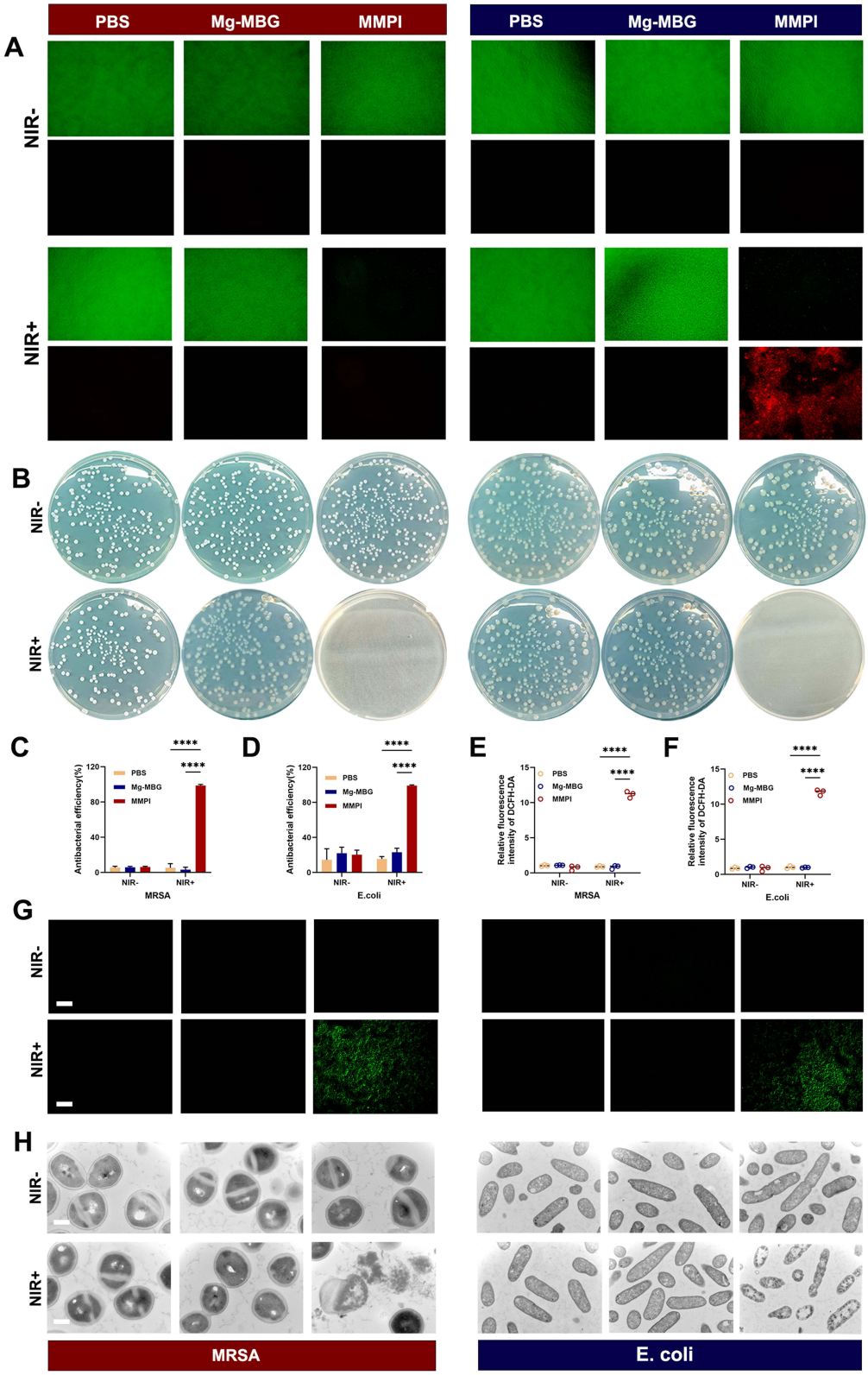

Figure 4 Antibacterial properties in vitro of various samples. (**A**) The fluorescence images of living bacterial (green) and dead bacterial (red). Scale bar: 100 μm. (**B**) Representative plates of MRSA and E. coli colonies formed by the bacteria with various samples after 24 h of culture. (**C**), (**D**) The bacterial inhibition rate of various samples. (**E**), (**F**) The fluorescence intensity analysis of various samples. (**G**) ROS release from various samples which co-cultured with bacteria with or without NIR irradiation. Scale bar: 100 μm. (**H**)Representative TEM images of MRSA (Scale bar: 10 μm) and E. coli (Scale bar: 20 μm) from biofilms after different treatments. ***P < 0.0001.

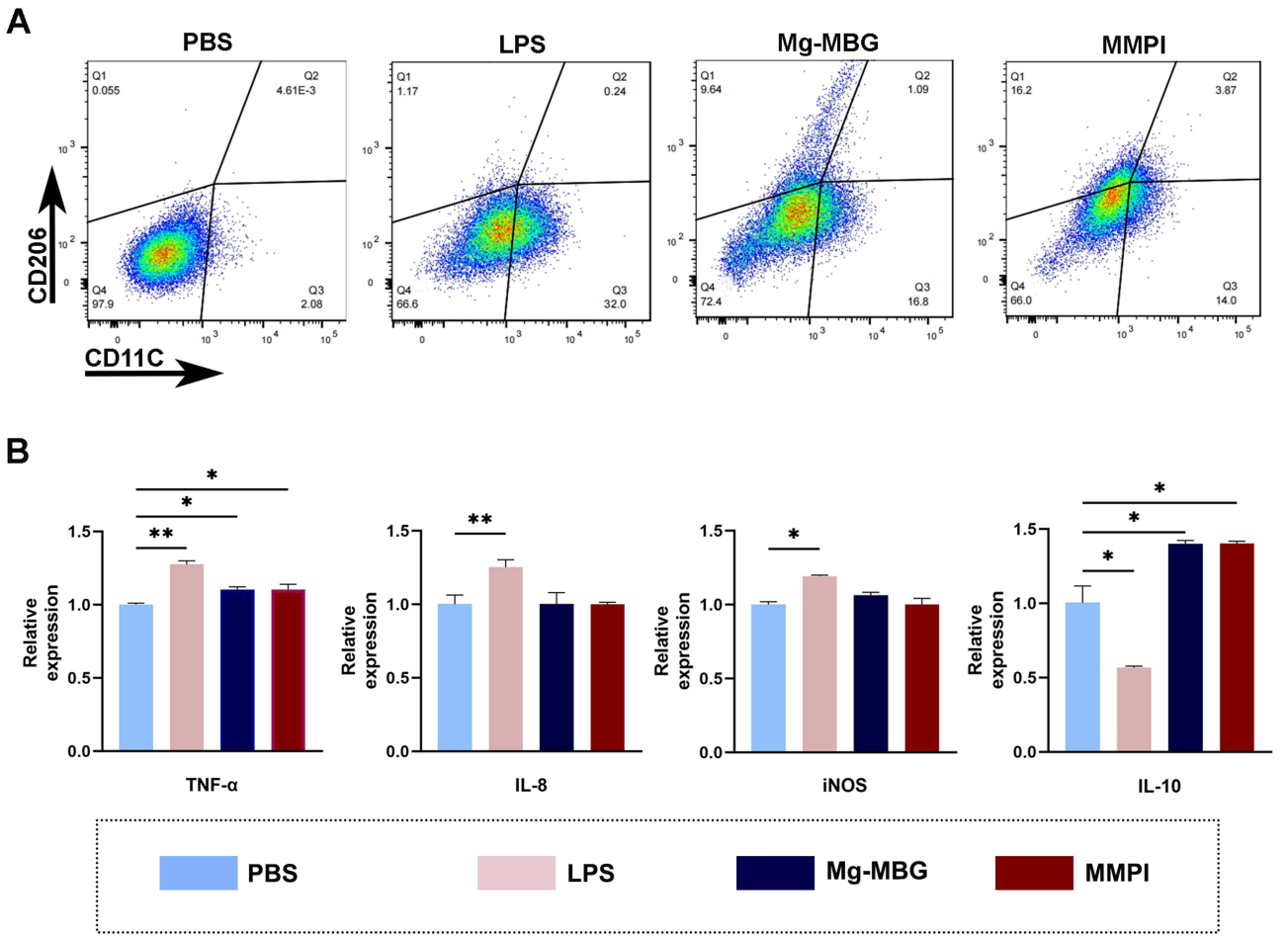

Figure 5 Immunomodulatory effects on macrophages in vitro. (**A**) Typical scatter plots of RAW264.7 macrophages surface markers CD11C (M1 macrophages marker) and CD206 (M2 macrophages marker) detected using flow cytometer. (**B**) RT-PCR detection of macrophage polarization and inflammation related gene expression. *P < 0.05, **P < 0.01.

notably reduced, while the anti-inflammatory gene IL-10 was upregulated after exposure to Mg-MBG and MMPI in comparison to the PBS and LPS groups. A prior investigation demonstrated that the presence of free Mg^{2+} suppressed the activation of inflammatory genes. Through a comparison of the results obtained from ICP, it was determined that the concentrations of Mg^{2+} released from Mg-MBG and MMPI were 5.4065 and 5.341 mg/L, respectively. Consequently, it is hypothesized that the immunomodulatory properties of Mg-MBG and MMPI may be attributed to the liberation of free Mg^{2+}.

In vivo Antibacterial Performance

The in vivo efficacy of MMPI in enhancing the healing process of infected wounds was further assessed. The methodology of the in vivo study is illustrated in Figure 6A. Initially, the infected wound was subjected to laser irradiation at a wavelength of 808 nm for 600 s, while the real-time temperature was monitored using a thermal camera to assess the photothermal conversion capabilities of MMPI in vivo. Figure 6B illustrates the temperature changes observed during the irradiation process, indicating an increase in temperature from 30.2 to 32.3°C for PBS, 30.4 to 32.9°C for Mg-MBG, and 36.1 to 45.4°C for MMPI after 300 s of irradiation. Subsequently, MMPI's temperature stabilized at 46.4°C after 600 s of irradiation, demonstrating greater variability compared to the other materials.

Subsequently, we utilized the skin excision infected mouse model to assess the impact of MMPI + NIR on infected wound healing. Analysis of the results depicted in Figure 6C revealed the presence of macroscopic infection, areas of tissue necrosis, and pus exudation in the wounds of the PBS, Mg-MBG, and MMPI groups on day 3. In contrast, the

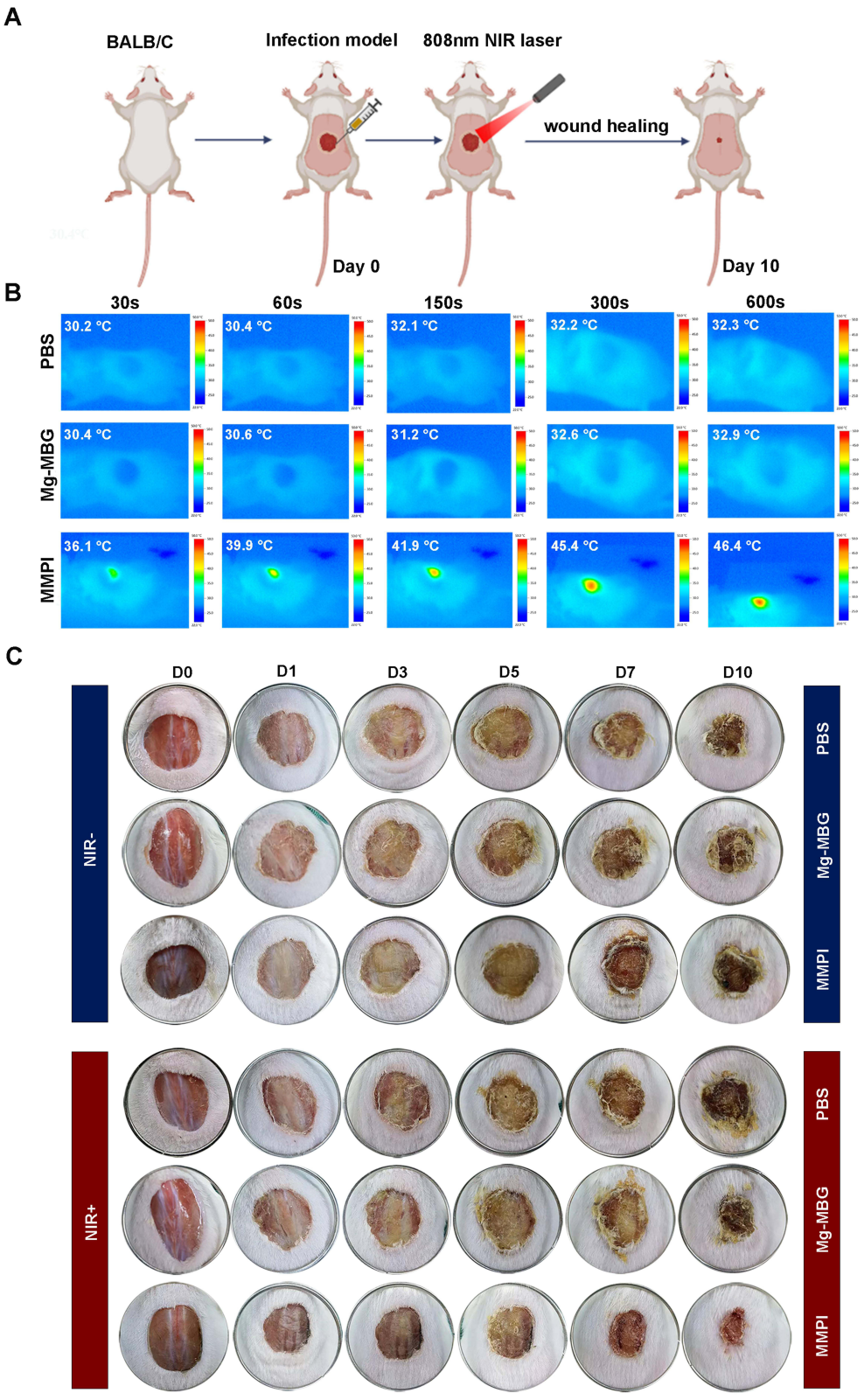

Figure 6 Antibacterial and photothermal performance in vivo. (**A**) Schematic diagram of infected wound formation and the following treatments. (**B**) Representative real-time thermographic images under NIR irradiation during 600 s. (**C**) Representative pictures of infected wounds during the wound healing process.

wounds in the MMPI + NIR group exhibited sustained cleanliness and dryness throughout the observation period, with no discernible signs of infection or sepsis. Furthermore, the wound healing process was accelerated in the MMPI + NIR-treated group compared to the other groups. Furthermore, samples of wound surface and surrounding tissues were obtained for histomorphometry analysis. The results depicted in Figure 7A indicated that, with the exception of the MMPI + NIR group, all other groups displayed a characteristic inflammatory reaction, as evidenced by significant inflammatory exudation and neutrophil infiltration observed through H&E staining. Conversely, the inflammatory

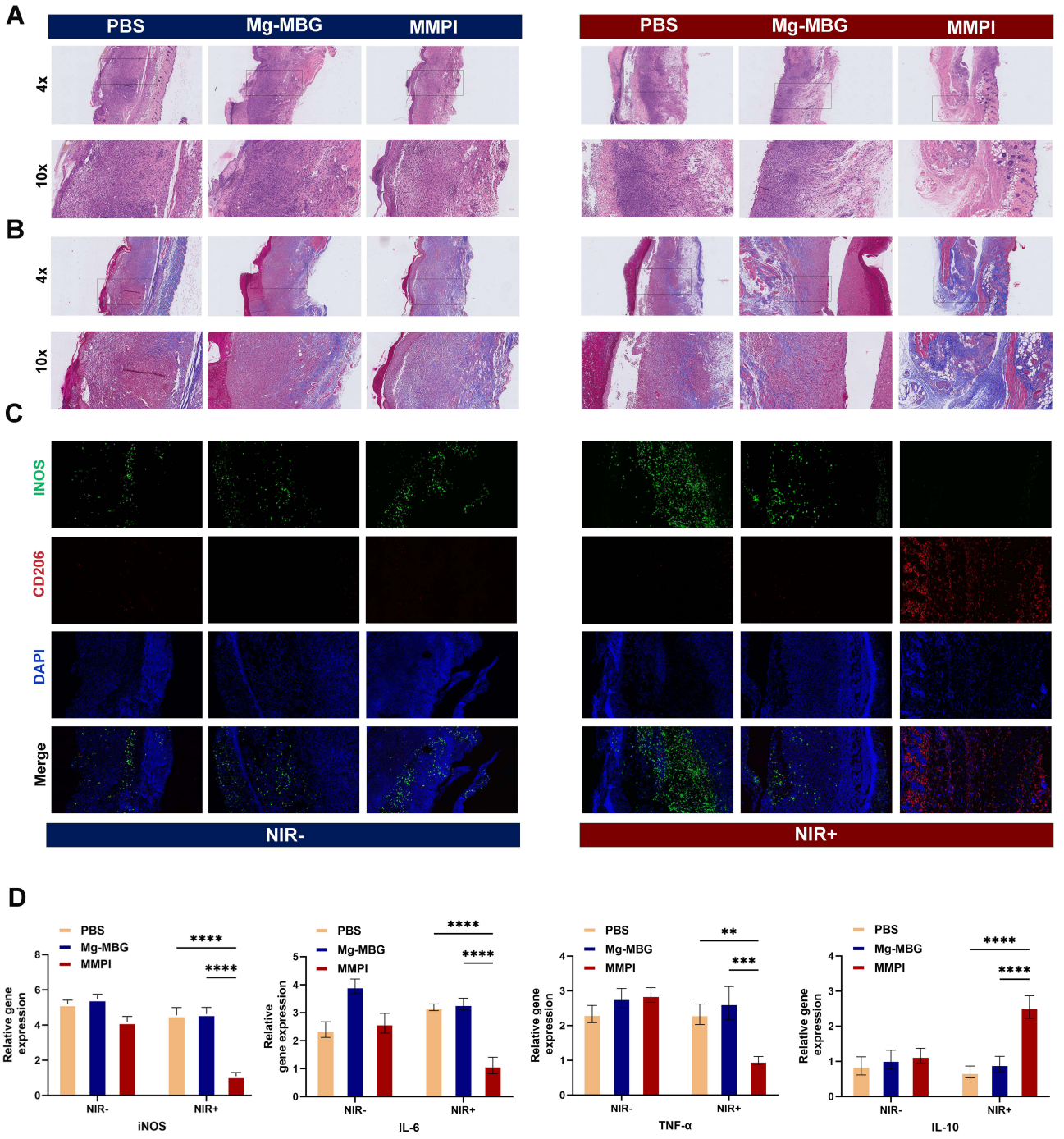

Figure 7 Histopathological examination of infected wounds after different treatments. (**A**) Representative HE staining images of skin tissues. (**B**) Representative Masson's trichrome (MT) staining images. (**C**) Immunofluorescent staining of skin tissues: green (iNOS), red (CD206), and blue (DAPI). (**D**) The inflammation related gene expression of wound tissue. **P < 0.01, ***P < 0.001, ****P < 0.0001.

response in the MMPI + NIR group was notably less severe. Additionally, infected wounds treated with MMPI + NIR exhibited enhanced collagen deposition, as illustrated in Figure 7B.

Macrophages serve as primary responders to tissue injury and play a crucial role in modulating the immune response to localized infections. Consequently, our study investigates the impact of various treatments on the immunomodulatory function of macrophages in the context of wound healing. In Figure 7C, the MMPI + NIR group exhibited the highest proportion of CD206 (M2 macrophages) and the lowest proportion of iNOS (M1 macrophages). In Figure 7D, the expression of the M1-associated macrophage genes (iNOS, IL-6 and TNF-α) were significantly decreased and that of M2-associated macrophage genes IL-10 increased in the wound treated with MMPI NIR+ on 10th day. These findings indicate that MMPI + NIR treatment may facilitate the polarization of macrophages towards the M2 phenotype, thereby suppressing the inflammatory response.

To elucidate the underlying mechanism, we conducted RNA-seq analysis on the wound skin of mice subjected to MMPI treatment in conjunction with NIR irradiation. Figure 8A demonstrates a strong correlation among

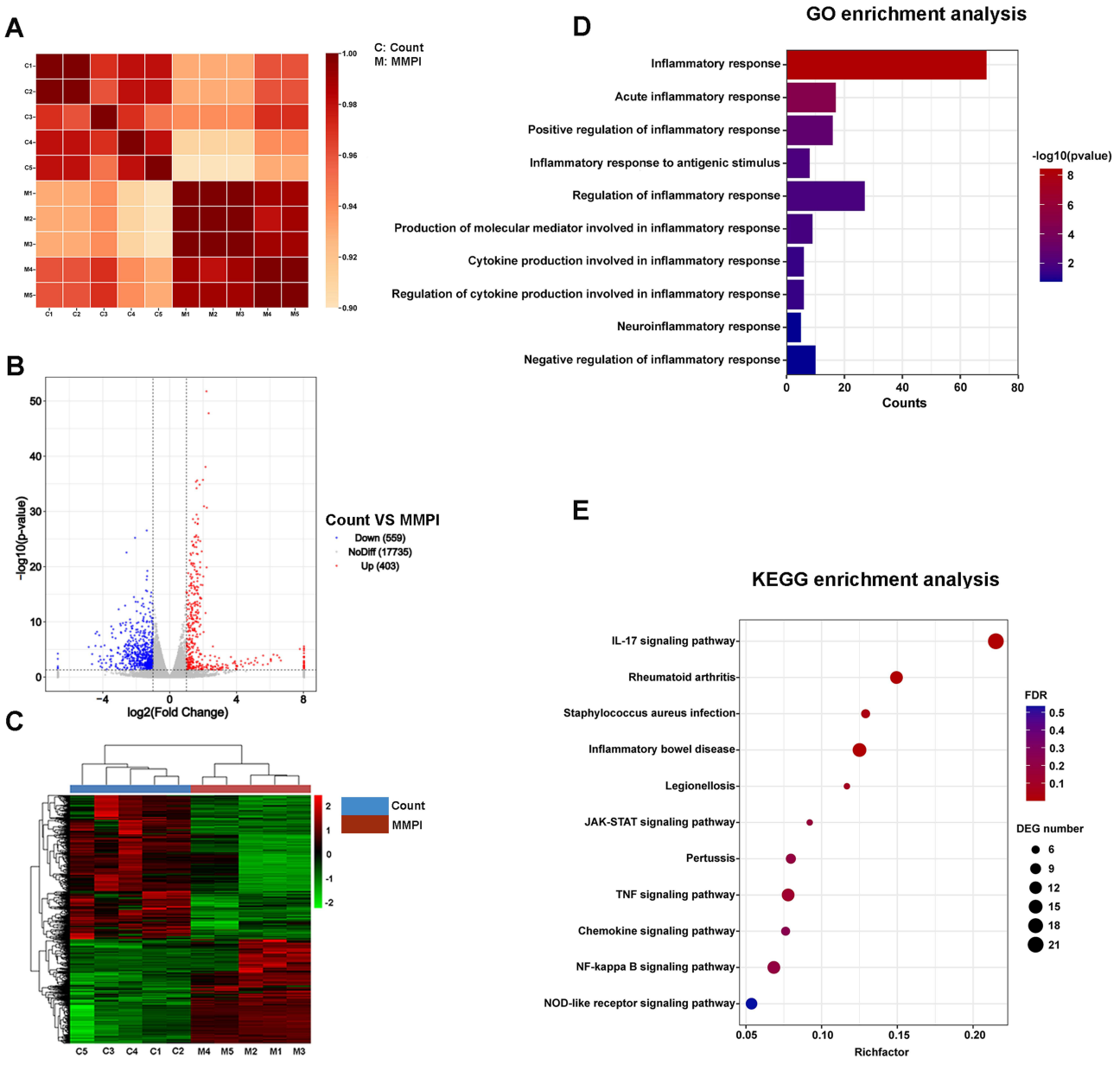

Figure 8 Exploration of anti-inflammatory mechanisms of MMPI by RNA-seq analysis in vivo. (**A**) FPKM distribution for all samples. (**B**) Volcano plots of DEGs. (**C**) Microarray heat map of all samples. (**D**) Biological process downregulated with MMPI samples were analyzed using the GO enrichment terms. (**E**) KEGG enrichment for the downregulated pathways of MMPI samples.

samples within each treatment group, indicating the reliability of the experiment and the rationality of sample selection. Subsequently, differentially expressed genes (DEG) were identified based on the criteria of P-value<0.05 and log2FoldChange > 1. In the MMPI + NIR group, a total of 962 DEGs were identified compared to the control group, with 403 being up-regulated and 559 being down-regulated (Figure 8B). Subsequently, the DEG heatmaps were generated by bidirectional clustering analysis of the union of differential genes and samples from all comparison groups (Figure 8C). The gene ontology (GO) enrichment analysis revealed that biological processes related to inflammation were predominantly down-regulated, particularly the inflammatory response (Figure 8D). Next, we performed the Kyoto Encyclopedia of Genes and Genomes (KEGG) pathway enrichment analysis, which indicated that pathways associated with inflammation were down-regulated in samples treated with MMPI. Specifically, the Interleukin-17 (IL-17) signaling pathway exhibited significant down-regulation following treatment with MMPI + NIR (Figure 8E). Thus, the findings from the RNA-seq analysis suggest that MMPI NIR+ treatment effectively suppresses the inflammatory response in wounds.

Conclusion

In this research, a novel nanoparticle (MMPI) was developed by coating Mg-MBG with PDA and loading it with ICG. The MMPI demonstrated both photothermal effects when exposed to NIR irradiation and effective antimicrobial properties in both in vitro and in vivo settings. The moderate high temperatures produced by NIR irradiation sensitized bacteria and facilitated the release of ROS from ICGs to eliminate susceptible bacteria. Furthermore, the incorporation of a PDA coating provided the samples with favorable cytocompatibility. Both in vitro and in vivo experiments demonstrate that MMPI enhances macrophage polarization towards the M2 phenotype and creates a favorable microenvironment for tissue regeneration. Furthermore, MMPI accelerates the healing process of infected wounds when exposed to NIR. These findings suggest that MMPI holds great potential as a novel nanoparticle for enhancing antimicrobial activity and promoting tissue repair.

Funding

This work was supported by the Science and Technology Innovation Plan of Shanghai Science and Technology Commission [Grant No.22S31900400] and the National Natural Science Foundation of China [Grant No. 81702666].

Disclosure

The authors declare that they have no known competing financial interests or personal relationships that could have appeared to influence the work reported in this paper.

References

1. Li R, Liu K, Huang X. et al. Bioactive materials promote wound healing through modulation of cell behaviors. *Adv Sci*. 2022;9(10):e2105152. doi:10.1002/advs.202105152
2. Xu M, Chen Z, Chen K, Ma D, Chen L, DiPietro LA. Phagocytosis of apoptotic endothelial cells reprograms macrophages in skin wounds. *J Immunol Regen Med*. 2021;1:12.
3. Tottoli EM, Dorati R, Genta I, Chiesa E, Pisani S, Conti B. Skin wound healing process and new emerging technologies for skin wound care and regeneration. *Pharmaceutics*. 2020;12(8):735. doi:10.3390/pharmaceutics12080735
4. Ocsoy I, Yusufbeyoglu S, Yılmaz V, McLamore ES, Ildız N, Ülgen A. DNA aptamer functionalized gold nanostructures for molecular recognition and photothermal inactivation of methicillin-Resistant Staphylococcus aureus. *Colloids Surf B*. 2017;159:16–22. doi:10.1016/j.colsurfb.2017.07.056
5. Wang S, Wang Y, Peng Y, Yang X. Exploring the antibacteria performance of multicolor Ag, Au, and Cu nanoclusters. *ACS Appl Mater Interfaces*. 2019;11(8):8461–8469. doi:10.1021/acsami.8b22143
6. Chen Y, Gao Y, Chen Y, Liu L, Mo A, Peng Q. Nanomaterials-based photothermal therapy and its potentials in antibacterial treatment. *J Control Release*. 2020;328:251–262.
7. Rippa AL, Kalabusheva EP, Vorotelyak EA. Regeneration of dermis: scarring and cells involved. *Cells*. 2019;8(6):607.
8. Jiang Y, Huang J, Xu C, Pu K. Activatable polymer nanoagonist for second near-infrared photothermal immunotherapy of cancer. *Nat Commun*. 2021;12(1):742. doi:10.1038/s41467-021-21047-0
9. He X, Lv Y, Lin Y, et al. Platinum nanoparticles regulated V(2)C MXene nanoplatforms with NIR-ii enhanced nanozyme effect for photothermal and chemodynamic anti-infective therapy. *Adv Mater*. 2024;36(25):e2400366. doi:10.1002/adma.202400366

10. He X, Qian Y, Wu C, et al. Entropy-mediated high-entropy mxenes nanotherapeutics: NIR-II-enhanced intrinsic oxidase mimic activity to combat methicillin-resistant staphylococcus aureus infection. *Adv Mater*. 2023;35(26):2211432. doi:10.1002/adma.202211432
11. He X, Hou J-T, Sun X, et al. NIR-II photo-amplified sonodynamic therapy using sodium molybdenum bronze nanoplatform against subcutaneous staphylococcus aureus infection. *Adv Funct. Mater*. 2022;32(38):2203964. doi:10.1002/adfm.202203964
12. He X, Dai L, Ye L, et al. A vehicle-free antimicrobial polymer hybrid gold nanoparticle as synergistically therapeutic platforms for staphylococcus aureus infected wound healing. *Adv Sci*. 2022;9(14):e2105223. doi:10.1002/advs.202105223
13. Bai X, Yang Y, Zheng W, Huang Y, Xu F, Bao Z. Synergistic photothermal antibacterial therapy enabled by multifunctional nanomaterials: progress and perspectives. *Mater Chem Front*. 2023;7(3):355–380. doi:10.1039/D2QM01141G
14. Liang J, Kang D, Wang Y, Yu Y, Fan J, Takashi E. Carbonate ion-enriched hot spring water promotes skin wound healing in nude rats. *PLoS One*. 2015;10(2):e0117106. doi:10.1371/journal.pone.0117106
15. Sheng L, Zhang Z, Zhang Y, et al. A novel hot spring mimetic hydrogel with excellent angiogenic properties for chronic wound healing. *Biomaterials*. 2021;264:120414. doi:10.1016/j.biomaterials.2020.120414
16. Yi X, Duan QY, Wu FG. Low-temperature photothermal therapy: strategies and applications. *Research*. 2021;2021:9816594. doi:10.34133/2021/9816594
17. Zheng D, Huang C, Zhu X, Huang H, Xu C. Performance of polydopamine complex and mechanisms in wound healing. *Int J Mol Sci*. 2021;22(19):10563. doi:10.3390/ijms221910563
18. He X, Obeng E, Sun X, Kwon N, Shen J, Yoon J. Polydopamine, harness of the antibacterial potentials-A review. *Mater Today Bio*. 2022;15:100329. doi:10.1016/j.mtbio.2022.100329
19. Yuan Z, Lin C, He Y, et al. Near-infrared light-triggered nitric-oxide-enhanced photodynamic therapy and low-temperature photothermal therapy for biofilm elimination. *ACS Nano*. 2020;14(3):3546–3562. doi:10.1021/acsnano.9b09871
20. Wang Z, Wang W, Wamsley M, Zhang D, Wang H. Colloidal polydopamine beads: a photothermally active support for noble metal nanocatalysts. *ACS Appl Mater Interfaces*. 2022;14(15):17560–17569. doi:10.1021/acsami.2c03183
21. Guo W, Ren Y, Chen Z, et al. Targeted magnetic resonance imaging/near-infrared dual-modal imaging and ferroptosis/starvation therapy of gastric cancer with peritoneal metastasis. *Adv Funct. Mater*. 2023;33(27):2213921. doi:10.1002/adfm.202213921
22. Higbee-Dempsey E, Amirshaghaghi A, Case MJ, Miller J, Busch TM, Tsourkas A. Indocyanine green-coated gold nanoclusters for photoacoustic imaging and photothermal therapy. *Advanced Therapeutics*. 2019;2(9). [*Adv Ther (Weinh).*]. doi:10.1002/adtp.201900088
23. Mahmut Z, Zhang C, Ruan F, et al. Medical applications and advancement of near infrared photosensitive indocyanine green molecules. *Molecules*. 2023;28(16):6085. doi:10.3390/molecules28166085
24. Wu J, Yang L, Li Y, Guo L. Research progress on mesoporous bioactive glass. *Sheng Wu Yi Xue Gong Cheng Xue Za Zhi*. 2018;35(4):647–650. doi:10.7507/1001-5515.201706091
25. Hooshmand S, Mollazadeh S, Akrami N, et al. Mesoporous silica nanoparticles and mesoporous bioactive glasses for wound management: from skin regeneration to cancer therapy. *Materials*. 2021;14(12):3337. doi:10.3390/ma14123337
26. Wu C, Chang J. Multifunctional mesoporous bioactive glasses for effective delivery of therapeutic ions and drug/growth factors. *J Control Release*. 2014;193:282–295. doi:10.1016/j.jconrel.2014.04.026
27. Chen B, Hong H, Sun Y, et al. Role of macrophage polarization in osteoarthritis (Review). *Exp Ther Med*. 2022;24(6):757. doi:10.3892/etm.2022.11693
28. Ashique S, Kumar S, Hussain A, et al. A narrative review on the role of magnesium in immune regulation, inflammation, infectious diseases, and cancer. *J Health Popul Nutr*. 2023;42(1):74. doi:10.1186/s41043-023-00423-0
29. Nielsen FH. Magnesium deficiency and increased inflammation: current perspectives. *J Inflamm Res*. 2018;11:25–34. doi:10.2147/JIR.S136742
30. Baino F, Fiorilli S, Vitale-Brovarone C. Composite biomaterials based on sol-gel mesoporous silicate glasses: a review. *Bioengineering*. 2017;4(1). doi:10.3390/bioengineering4010015
31. Li Y, Gong T, Gao H, et al. ZIF-based nanoparticles combine X-ray-induced nitrosative stress with autophagy management for hypoxic prostate cancer therapy. *Angew Chem Int Ed*. 2021;60(28):15472–15481. doi:10.1002/anie.202103015
32. Ou Q, Zhang S, Fu C, et al. More natural more better: triple natural anti-oxidant puerarin/ferulic acid/polydopamine incorporated hydrogel for wound healing. *J Nanobiotechnol*. 2021;19(1):237. doi:10.1186/s12951-021-00973-7
33. Feng K, Peng L, Yu L, et al. Universal antifogging and antimicrobial thin coating based on dopamine-containing glycopolymers. *ACS Appl Mater Interfaces*. 2020;12(24):27632–27639. doi:10.1021/acsami.0c07949
34. Su X, Lyu Z, Wu Y, Gu Y-H, Huo S, Zhou C. Strontium-doped bioactive glass/PDA functionalized polyetheretherketone with immunomodulatory property for enhancing photothermal clearance of Staphylococcus aureus. *Mater Des*. 2023;1:225.
35. Qi X, Huang Y, You S, et al. Engineering robust ag-decorated polydopamine nano-photothermal platforms to combat bacterial infection and prompt wound healing. *Adv Sci*. 2022;9(11):2106015. doi:10.1002/advs.202106015
36. Heise S, Höhlinger M, Hernández YT, et al. Electrophoretic deposition and characterization of chitosan/bioactive glass composite coatings on Mg alloy substrates. *Electrochim Acta*. 2017;232:456–464. doi:10.1016/j.electacta.2017.02.081
37. Sitarz M, Handke M, Fojud Z, Jurga S. Spectroscopic studies of glassy phospho-silicate materials. *J Mol Struct*. 2005;744-747:621–626. doi:10.1016/j.molstruc.2004.12.050
38. Ma H, Luo J, Sun Z, et al. 3D printing of biomaterials with mussel-inspired nanostructures for tumor therapy and tissue regeneration. *Biomaterials*. 2016;111:138–148. doi:10.1016/j.biomaterials.2016.10.005
39. Gao G, Jiang Y-W, Jia HR, F-G W. Near-infrared light-controllable on-demand antibiotics release using thermo-sensitive hydrogel-based drug reservoir for combating bacterial infection. *Biomaterials*. 2019;188:83–95. doi:10.1016/j.biomaterials.2018.09.045
40. Kyriakides TR, Raj A, Tseng TH, et al. Biocompatibility of nanomaterials and their immunological properties. *Biomed Mater*. 2021;16(4):1.
41. Kim H, Wang SY, Kwak G, Yang Y, Kwon IC, Kim SH. Exosome-guided phenotypic switch of M1 to M2 macrophages for cutaneous wound healing. *Adv Sci*. 2019;6(20):1900513. doi:10.1002/advs.201900513
42. Spiller KL, Nassiri S, Witherel CE, et al. Sequential delivery of immunomodulatory cytokines to facilitate the M1-to-M2 transition of macrophages and enhance vascularization of bone scaffolds. *Biomaterials*. 2015;37:194–207.
43. Brauneck F *et al*. (2022). TIGIT blockade repolarizes AML-associated TIGIT + M2 macrophages to an M1 phenotype and increases CD47-mediated phagocytosis. J Immunother Cancer. 10(12): e004794. doi: 10.1136/jitc-2022-004794

44. Xie Y, Li H, Xu L, et al. DNA nanoclusters combined with one-shot radiotherapy augment cancer immunotherapy efficiency. *Adv Mater*. 2023;35 (17):2208546. doi:10.1002/adma.202208546
45. Zhou C, Weng J, Liu C, et al. Disruption of SLFN11 deficiency-induced CCL2 signaling and macrophage M2 polarization potentiates anti-PD-1 therapy efficacy in hepatocellular carcinoma. *Gastroenterology*. 2023;164(7):1261–1278.